Geophysical Journal International

Geophys. J. Int. (2017) **209,** 866–875
Advance Access publication 2017 February 17
GJI Seismology

doi: 10.1093/gji/ggx056

Dynamic inversion of the 2015 Jujuy earthquake and similarity with other intraslab events

Carlos Herrera,[1] Sergio Ruiz,[1] Raúl Madariaga[2] and Piero Poli[3]

[1]*Departamento de Geofísica, Universidad de Chile,* 8370449 *Santiago, Chile. E-mail: carlosfherrera@ug.uchile.cl*
[2]*Laboratoire de Géologie, Centre National de la Recherche Scientifique, École Normale Supérieure, F-*75231 *Paris Cedex* 5*, France*
[3]*Department of Earth, Atmospheric and Planetary Sciences, Massachusetts Institute of Technology, Cambridge, MA* 02139-4307*, USA*

Accepted 2017 February 14. Received 2017 February 9; in original form 2016 September 8

SUMMARY

We study the seismic source of the 2015 (M_w 6.7) Jujuy, Argentina intermediate depth earthquake. We first constrain the fault plane by using a teleseismic inversion and by determining the aftershock distribution. Then, we perform kinematic and dynamic inversions to retrieve the parameters that control the rupture process, using data at regional distances, and modelling the source as an elliptical patch. Best models suggest a subshear rupture propagation with a duration of ∼5 s. Results from the dynamic modelling suggest a stress drop of 11.87 MPa and a fracture energy rate of 2.95 MJ m^{-2}, which are slightly less but of the same order as those of other events of similar size. Finally, we perform a Monte-Carlo inversion to explore the behaviour of the frictional parameters in the solution space, and then we compare our results with other intraslab events. We find that the κ parameter (ratio between strain energy and fracture energy) and the relation between seismic moment and stress drop are similar for all the considered events.

Key words: Numerical modelling; Body waves; Computational seismology; Earthquake dynamics; Earthquake source observations.

1 INTRODUCTION

The convergent margin of the Nazca and South American plates exhibits a constant seismic activity in a wide range of depths, which distribution has been widely used to study the shape of the plate contact and tectonic structure (e.g. Cahill & Isacks 1992; Comte *et al*. 1994). Shallow earthquakes generally occur due to brittle fractures on the fault systems. But with the increase of pressure and temperature with depth, brittle rupture is inhibited below ∼30–50 km. Yet, along this convergent margin earthquakes can occur down to a depth of 700 km, and their main characteristics suggest a brittle rupture easily explained as shear-slip on faults, just as shallow crustal earthquakes. These deep seismic events differ from crustal events, when radiated seismic energy (Wiens 2001; Poli & Prieto 2016), and source durations (Campus & Das 2000; Frohlich 2006; Poli & Prieto 2014; Houston 2015) are considered. Detailed comparison between deep earthquakes shows a large diversity of rupture behaviour (Wiens 2001; Poli & Prieto 2014, 2016), with mainly slow rupture velocity and low efficiency events observed in warm subducted slabs, and faster more energetic ruptures in cold slabs (Kanamori *et al*. 1998; Chen *et al*. 2014; Zhan *et al*. 2014; Poli *et al*. 2016).

Among the wide range of deep earthquakes, the events that occur between 70 and 350 km depth are called intermediate depth earthquakes (Houston 2015). The rupture process of this kind of earthquakes has been studied in other regions using teleseismic data (Houston *et al*. 1998; Tocheport *et al*. 2007; Poli & Prieto 2014), or using regional data with kinematic and dynamic models (e.g. Peyrat & Favreau 2010; Ruiz & Madariaga 2013).

The dynamic rupture inversion (Peyrat *et al*. 2001; Di Carli *et al*. 2010; Ruiz & Madariaga 2011, 2013; Díaz-Mojica *et al*. 2014; Twardzik *et al*. 2014) permits us to study the parameters that generate the rupture, which are regulated by a certain friction law (e.g. Ruiz & Madariaga 2011), thus giving us unique information about the physics of intermediate depth faulting.

A group of intermediate depth earthquakes occurred during 2014 and 2015 in the region of Jujuy, in Argentina, which is marked inside the red squares in Fig. 1. The largest of them had a magnitude M_w 6.7 (USGS) and occurred in February 2015. We called this event the Jujuy earthquake.

To gain more insights about the properties of intermediate depth earthquakes, in this paper we study the rupture process of the 2015 Jujuy earthquake. As in previous work (Vallée & Bouchon 2004), we make use of an elliptical rupture patch to model the slip distribution, and focus on detailed derivation of rupture and frictional parameters. To limit the parameters to be explored during the inversions, we first estimated the rupture velocity using teleseismic *P* waves. Then, we performed a kinematic inversion, using broadband records at regional distances (Fig. 2). We finally implemented a full dynamic inversion and a Monte-Carlo search to study the frictional

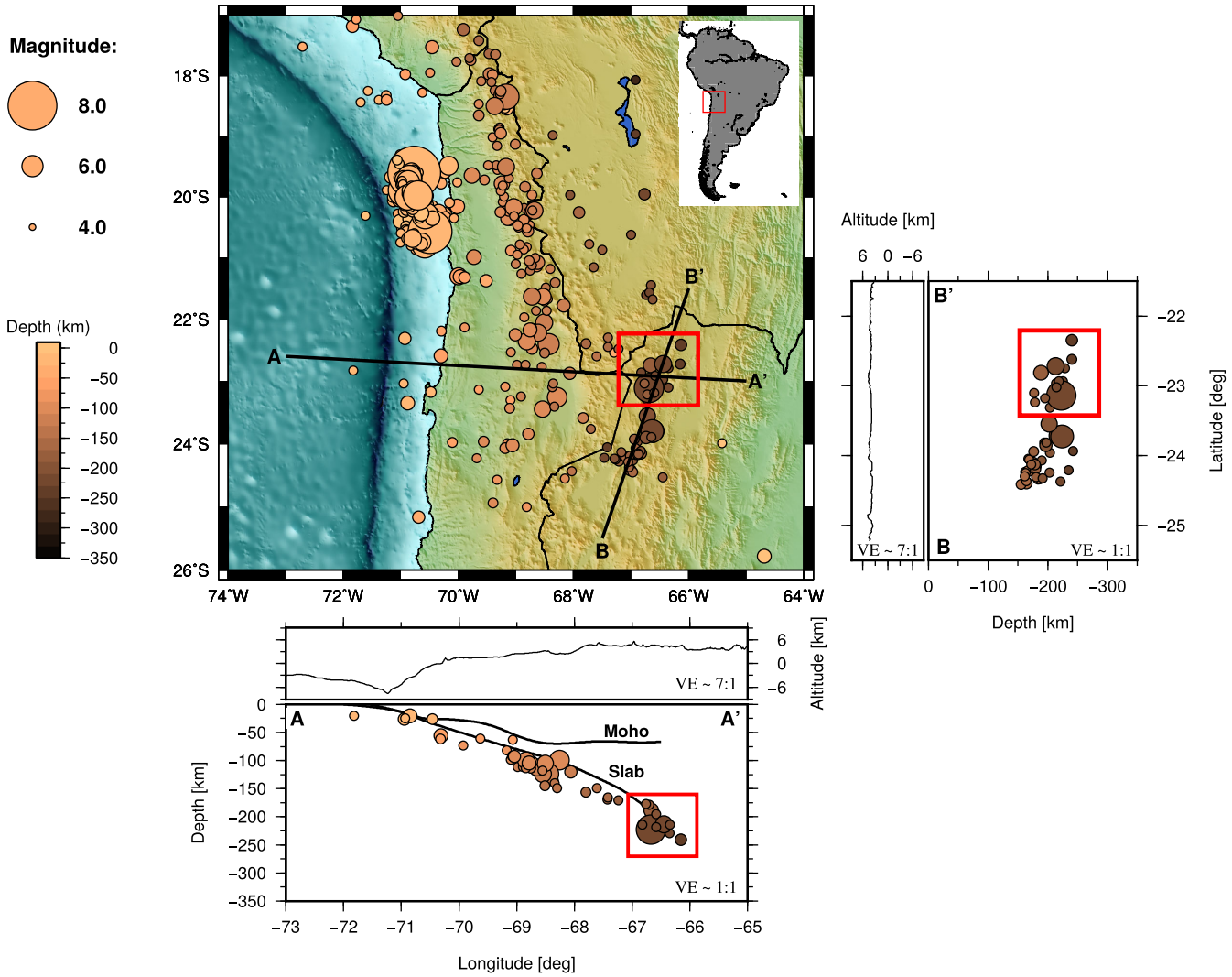

Figure 1. Seismicity with magnitudes higher than 4.5 in northern Chile between 2014 January 1 and 2015 November 1. The locations of the hypocentres were obtained from the USGS catalogue. The red boxes in the map and the cross-sections indicate the cluster of events where the Jujuy earthquake is located. The slab and moho models were obtained by Tassara & Echaurren (2012) and are shown only as a tectonic reference.

parameters, and compare our results with other intraslab events in Chile and Japan. The hypocentre of the Jujuy earthquake is located deeper than 200 km, making this event the deepest one for which a dynamic inversion has been made to obtain the friction parameters that control the rupture process.

2 THE JUJUY EARTHQUAKE AND AVAILABLE DATA

The Jujuy earthquake (M_w 6.7) occurred on 2015 February 11 at 18:57:22 (UTC) under the Jujuy province of Argentina. This event was well recorded by broadband stations in the region (Fig. 2). We located the hypocentre of the main-shock using the NonLinLoc program (Lomax *et al*. 2000) with the 1-D velocity model proposed by Husen *et al*. (1999) at 23.117°S, 66.807°W and 254 km depth, with residuals of 1.67, 1.45 and 3.44 km in the east, north and vertical components, respectively, and a global RMS of 0.31. In general, we observe differences between the hypocentres reported by several agencies. USGS, GEOFON and Centro Sismológico Nacional (CSN) suggest depths of 223, 198 and 239 km respectively. To check our result, we also located the aftershocks ($M_w \geq 3.5$) that occurred during the first month after the main event, using NonLinLoc with the same 1-D velocity model. The obtained locations of the aftershocks are in agreement with our location of the main shock (see Fig. 2). We also performed some tests with the kinematic inversion described in the following sections, using as input different hypocentres, and we found that the best fit to the observed data was obtained by using our location of the hypocentre (see Supporting Information Fig. S1).

This earthquake had a normal-fault focal mechanism (NP1: strike 176°, dip 19°, rake −93°. NP2: strike 359°, dip 71°, rake −88°) as reported by the GEOFON agency. The resulting distribution of aftershocks from the location process shows a trend along the subvertical plane (NP2) (Fig. 2), suggesting that the rupture occurred along that plane. To corroborate this hypothesis, we also studied the directivity of teleseismic *P* waves using the stretching technique and a Grid-Search inversion (Warren & Silver 2006) to get the plane dip, rupture azimuth and rupture velocity. The results of the teleseismic directivity inversion show that the rupture took place along a subvertical plane, with a rupture velocity of 2.8 km s^{-1} (see Supporting Information Text S1 and Fig. S2 for more details).

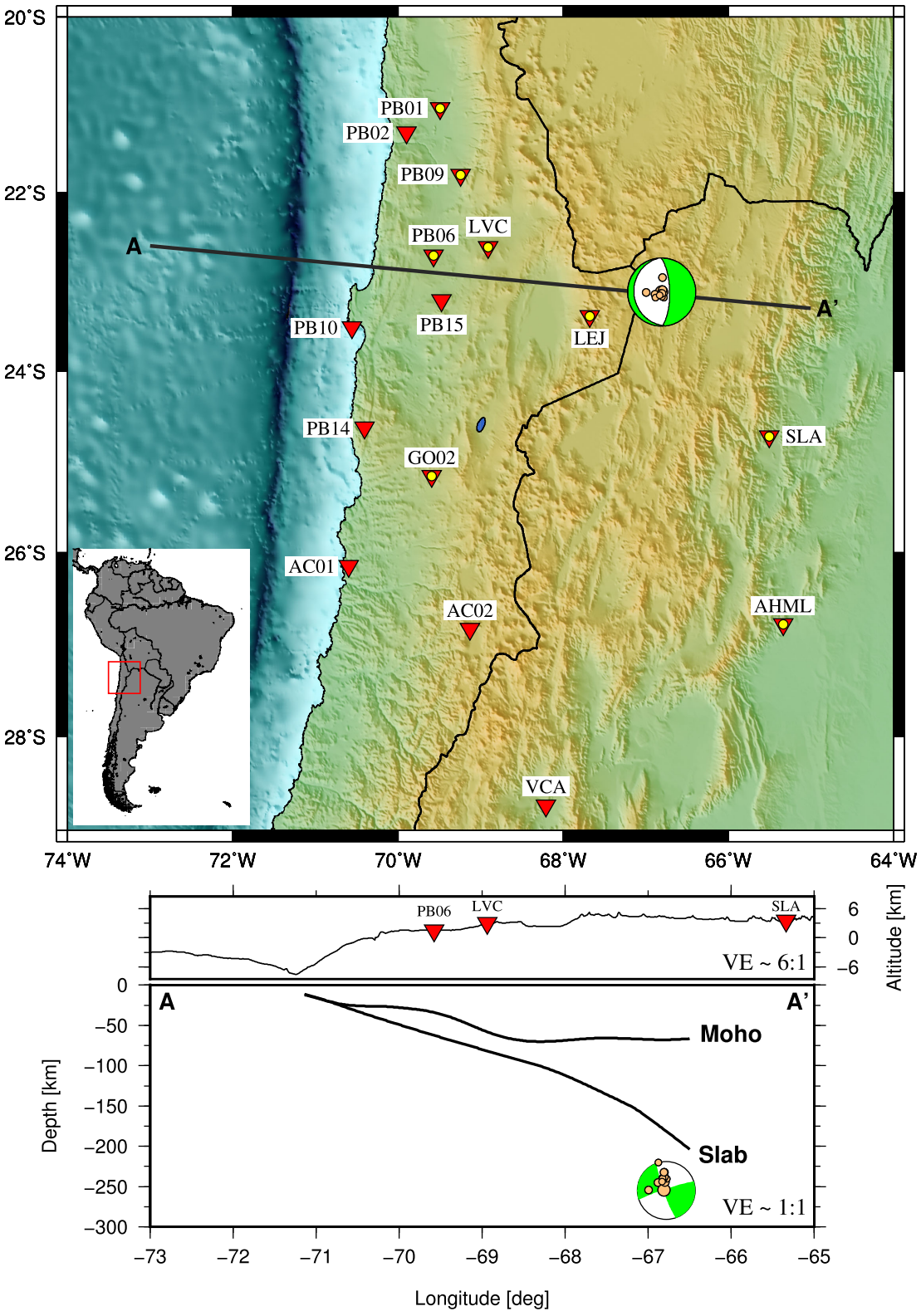

Figure 2. Location of the Jujuy earthquake and stations used. Stations with available data for our analysis are shown with red triangles, while the stations used for inversion are marked with yellow circles. The shown focal mechanism was calculated by GEOFON. The small light brown circles are the located aftershocks. The slab and moho sections were proposed by Tassara & Echaurren (2012) and are shown only as a tectonic reference.

For the inversions with regional data, we used the broadband channels of stations located as close as possible to the epicentre (stations marked with yellow circles in Fig. 2). The observed records and synthetic time series obtained from the inversion were filtered between 0.02 and 0.12 Hz using a causal bandpass Butterworth filter of order 2. The low-frequency limit was chosen to avoid the noise at the edge of the instrumental response because we concentrated our analysis in the flat part of the instrumental spectrum. The

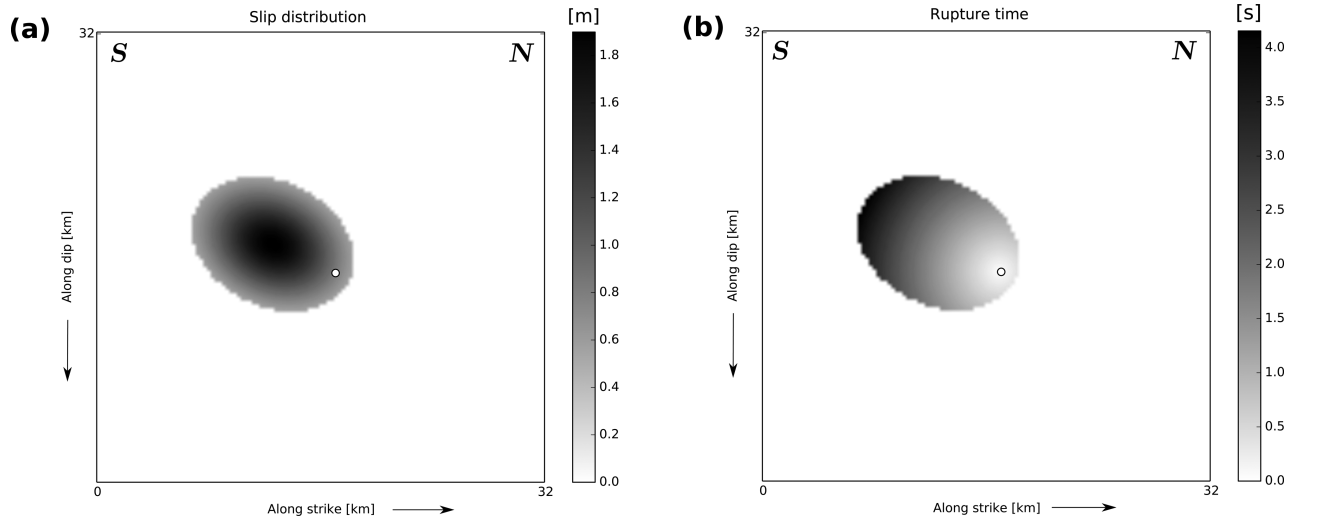

Figure 3. Best kinematic model obtained by the Neighbourhood Algorithm. (a) Slip distribution. (b) Rupture time isochrones. The hypocentre is marked with the white circle. Letters S and N show the approximate orientations of south and north directions, respectively.

high-frequency limit is controlled by our simple elliptical model and the 1-D velocity model (Husen *et al*. 1999) used to simulate the wave propagation from the source to the receivers. Initially we performed the inversion using different high-frequency limits at 0.2, 0.25 and 0.5 Hz. Unfortunately, at frequencies higher than 0.12 Hz, the observed seismograms are controlled by local site effects that cannot be reproduced by our synthetic records, generating large errors that can put into question the fit of the model to the observed data (misfits of 0.48, 0.54, 0.69 for frequencies up to 0.2, 0.25 and 0.5 Hz, respectively). See Supporting Information Figs S3–S5.

3 METHODOLOGY

To model the source with data at regional distances we used a single elliptical patch, because we are interested in exploring the average characteristics of the seismic rupture in low frequencies. We used two approaches to model the rupture process of the Jujuy earthquake: a kinematic and a dynamic model. The kinematic model is described by seven parameters. Five of them are geometric parameters, which are the semi-axes a and b of the ellipse, the rotation angle of the ellipse α and the location (x_0, y_0) of its centre inside the fault plane, while the other two parameters are kinematic and describe the maximum slip $D_{\max}$ and the rupture velocity V_r. The dynamic model has 10 parameters. In addition to the geometric parameters of the kinematic model, this model considers a circular nucleation of radius R' with a stress T_u' acting inside it, and the frictional parameters T_e, T_u and D_c, which are the stress drop, the yield stress and the slip weakening distance, respectively. Those frictional parameters are related by the linear decay friction law proposed by Ida (1972). A detailed description of kinematic and dynamic models and their inversion procedures can be found in Text S2 and Text S3 of the Supporting Information, respectively.

The AXITRA code (Bouchon 1981; Coutant 1989) was used to simulate the wave propagation from the source to the receivers, using the 1-D velocity model proposed by Husen *et al*. (1999) for northern Chile. The misfit χ^2 between observed and synthetic records generated for each of the tested models was calculated using the norm

$$\chi^2 = \frac{\sum_i (\mathrm{obs}_i - \mathrm{synth}_i)^2}{\sum_i \mathrm{obs}_i^2} \qquad (1)$$

where 'obs' are the observed records and 'synth' are the synthetic records. The sum runs over the samples of each seismogram in a particular window around *P* and *SH* waves.

For both kinematic and dynamic approaches, we modelled the seismic rupture following the methodology used by Ruiz & Madariaga (2013), performing inversions using the Neighbourhood Algorithm (Sambridge 1999) to find the optimal model that best fits the observed data. For the dynamic modelling, we also calculated the similarity parameter κ (Madariaga & Olsen 2000), for each explored model. κ is defined as

$$\kappa = \frac{(T_e - T_r)^2}{\mu\,(T_u - T_r)}\,\frac{L}{D_c} \qquad (2)$$

where L is the characteristic size of the rupture area, μ is the shear modulus (we used $\mu = 7.83 \times 10^{10}$ Pa, derived from the 1-D velocity model), T_r is the residual friction, which we assumed to be zero (see Supporting Information Text S3), and T_e, T_u and D_c were already defined. κ is roughly the ratio of available strain energy to the frictional energy release rate, and controls the overall characteristics of the rupture process (Madariaga & Olsen 2000). As we are studying the general characteristics of the source, we considered L as the mean of the semi-axes of each elliptical model tested.

We finally performed a Monte-Carlo inversion to explore the behaviour of the κ parameter and the other frictional parameters in the solution space.

4 KINEMATIC AND DYNAMIC INVERSION RESULTS

4.1 Neighbourhood Algorithm

We first performed a kinematic inversion to constrain the search intervals of the semi-axes a and b that will be used in the dynamic inversion, and to get the rupture velocity. We used the Neighbourhood Algorithm to obtain the model that best fits the data. The inversion converged stably to a minimum misfit of $\chi^2 = 0.35$ after exploring more than 2130 models. The best model is represented by an ellipse where the rupture propagates up and south from the hypocentre with a subshear rupture velocity of 2.4 km s^{-1} (see Supporting Information Table S1 for full details), which is consistent with the rupture velocity obtained by the teleseismic inversion. Fig. 3 shows the best

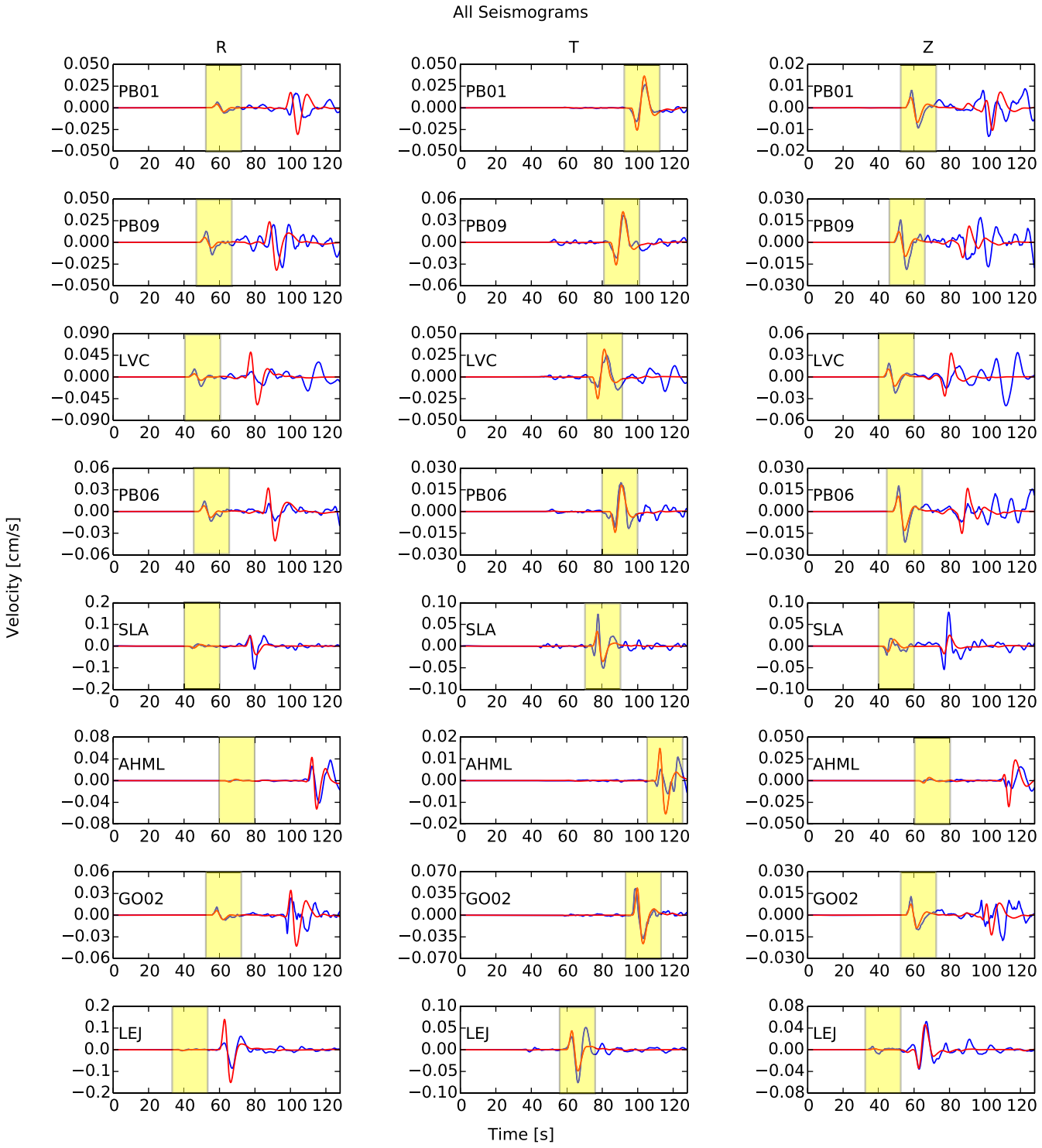

Figure 4. Comparison between observed (blue) and synthetic (red) seismograms of the best model obtained by the kinematic inversion using the Neighbourhood Algorithm. In this figure are shown all components and stations used in the inversion. Letters R, T and Z correspond to radial, transverse and vertical components, respectively. The yellow rectangles show the 20 s sections modelled around *P* waves in radial and vertical components and *SH* waves in the transverse component.

kinematic model, which has a modelled seismic moment of 7.14×10^{18} Nm, corresponding to $M_w = 6.5$.

Due to the limitations of the 1-D velocity model that we used, we calculated the misfit χ^2 only for *P* and *SH* waves. Fig. 4 shows the comparison between observed and synthetic seismograms of all stations considered in the inversion. It is clear that synthetic *P* and *SH* waves fit the observed records with an acceptable level of accuracy, but the rest of the waves were barely modelled.

For the dynamic modelling, our inversion converged stably to a minimum misfit after exploring more than 13 500 models. The model that best fits the observed data has a misfit of $\chi^2 = 0.4$, and was calculated again considering only *P* and *SH* waves, because the Green's functions were calculated using the same velocity model

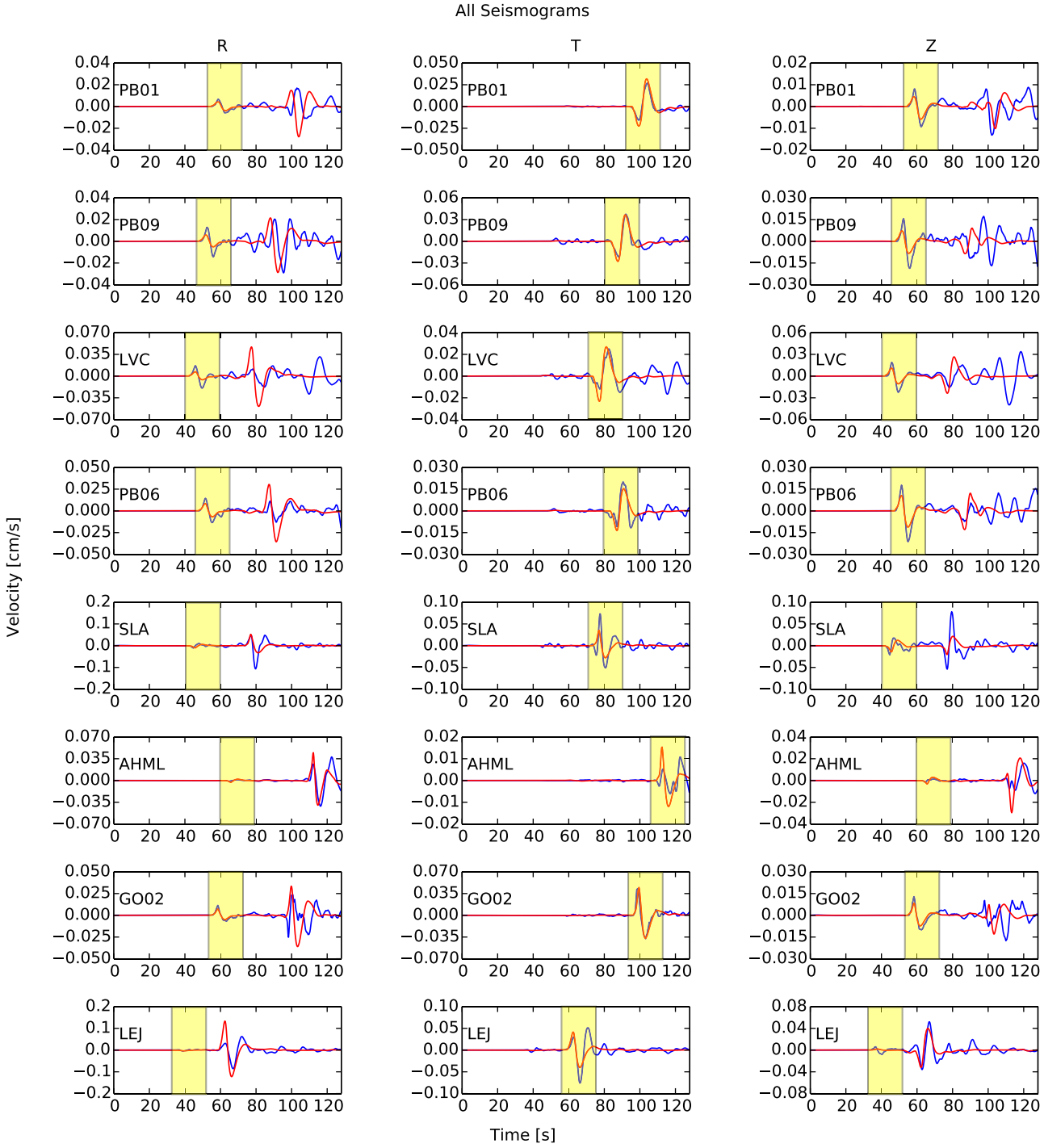

Figure 5. Comparison between observed (blue) and synthetic (red) seismograms of the best model obtained by the dynamic inversion using the Neighbourhood Algorithm. In this figure are shown all components and stations used in the inversion. Letters R, T and Z correspond to radial, transverse and vertical components, respectively. The yellow rectangles show the 20 s sections modelled around *P* waves in radial and vertical components and *SH* waves in the transverse component.

of the kinematic case. Fig. 5 shows the comparison between the observed and synthetic seismograms of the dynamic modelling. The 10 inverted parameters of the dynamic model are listed in Table 1, which shows the values for the best model and the search intervals.

Fig. 6(a) shows the slip distribution of the best solution, which has a modelled seismic moment of 6.69×10^{18} Nm (M_w 6.5). The elliptical patch is oriented up and south with respect to the hypocentre, which is in agreement with the result obtained from kinematic inversion, the teleseismic *P* waves and aftershock locations. In Fig. 6(b) we show the rupture propagation, which starts from the hypocentre and move upwards until 2.25 s, when the rupture front reaches the border of the elliptical patch. Then, it changes its direction to the south to finish its propagation in the southern limit of the ellipse after 5 s of propagation. This rupture duration agrees with the

Table 1. 10 inverted parameters that define the dynamic model. The inversion was made using the Neighbourhood Algorithm.

	a (km)	b (km)	x_0 (km)	y_0 (km)	α (rad)	T_e (MPa)	T_u (Mpa)	T_u' (MPa)	R' (km)	D_c (m)
Best model	7.94	4.87	12.71	11.63	3.55	11.87	14.37	16.10	1.09	0.41
Range minimum	3	3	6	6	0	8	8.4	8.82	0.8	0.4
Range maximum	9	9	26	26	6.28	35	52.5	78.75	1.6	1.6

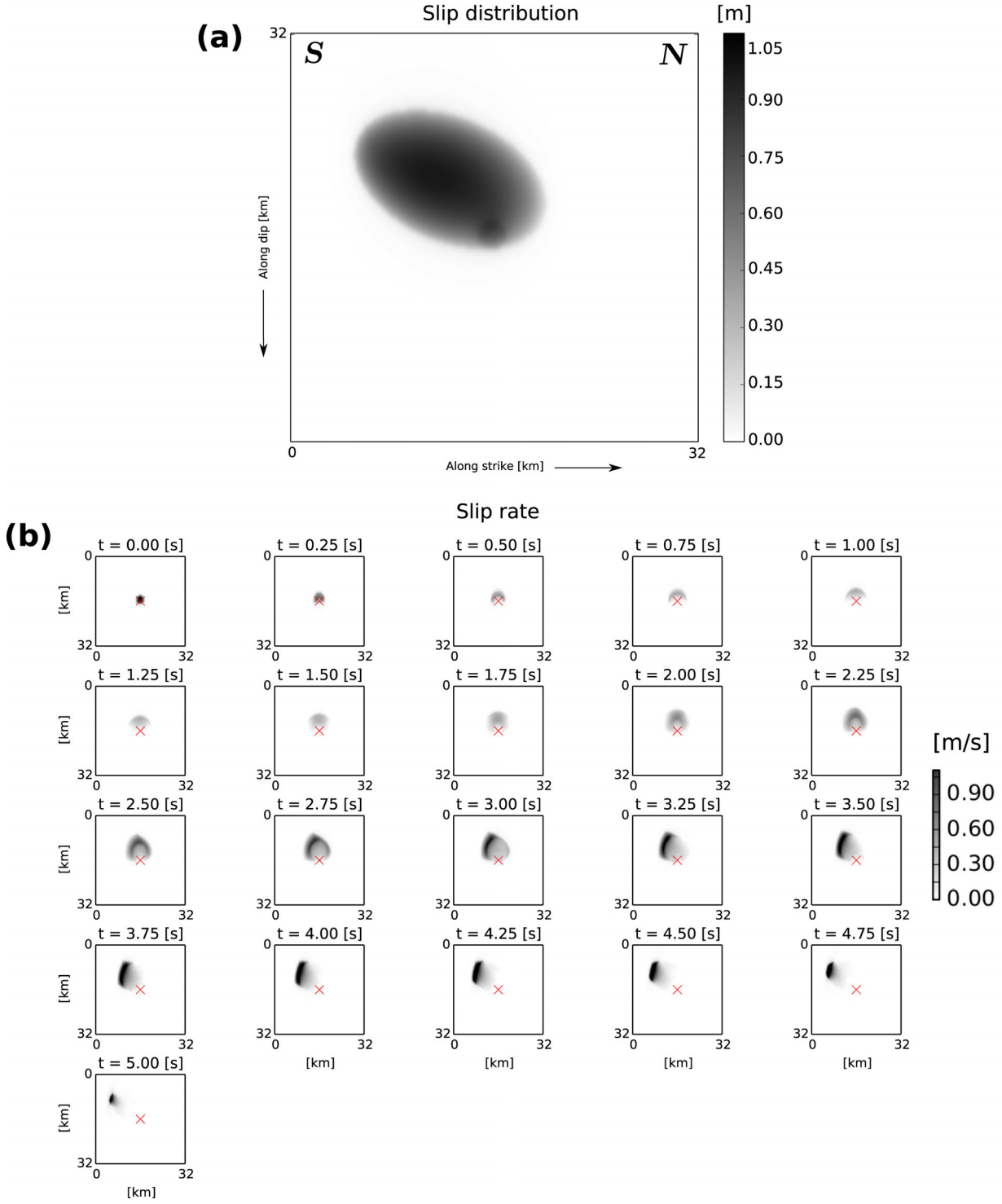

Figure 6. (a) Slip distribution of the best dynamic model obtained by the Neighbourhood Algorithm. The hypocentre is located at the centre inside the nucleation circle. S and N show the approximate orientations of south and north directions, respectively. (b) Slip rate snapshots showing the propagation of the rupture front each 0.25 s. The red cross indicates the hypocentre.

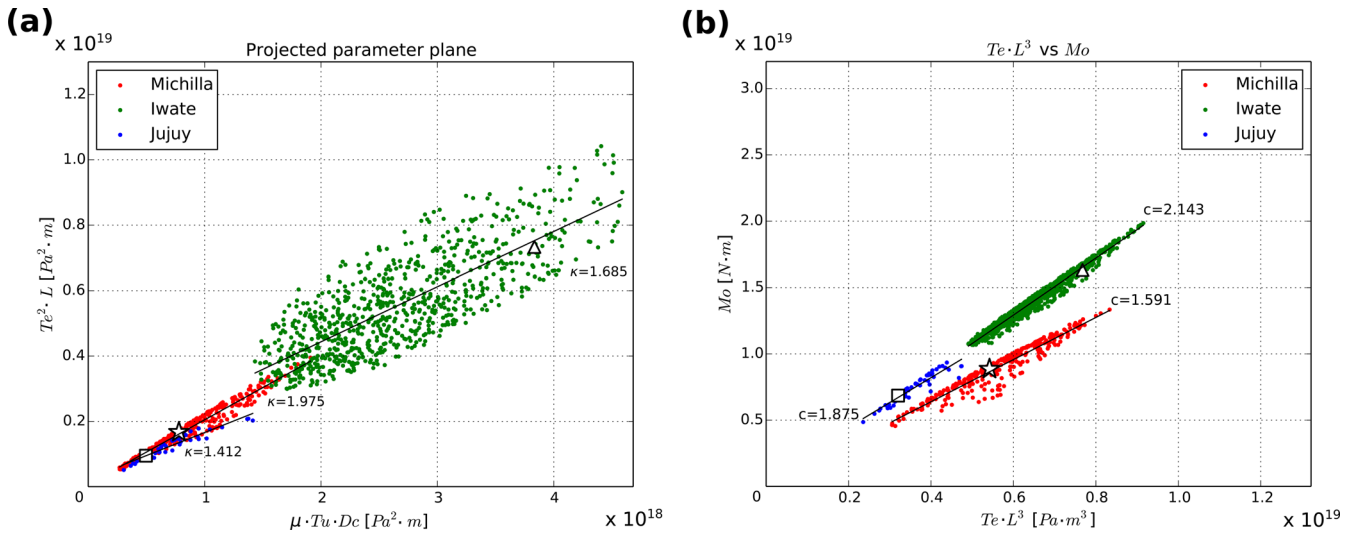

Figure 7. Monte-Carlo inversions of the Jujuy, Iwate and Michilla earthquakes. The models shown have misfits lower than 0.48. (a) Results projected in the plane ($\mu T_u D_c$, $T_e{}^2 L$). (b) Results projected in the plane ($T_e L^3$, M_o). The white square, star and triangle are the best models obtained by the Neighbourhood Algorithm for Jujuy, Michilla and Iwate earthquakes, respectively. The linear regressions that adjust the three model distributions and their slopes are shown in each graphic, with their respective slopes κ and c.

teleseismic measurements made from stacking of *P* waves for deep and intermediate depth earthquakes (Poli & Prieto 2016). The large values of slip rate are concentrated in the rupture front and in the edges of the ellipse, due to the stopping phases that are radiated when the rupture front reaches the limits of the elliptical patch. The inverted stress drop of the best dynamic model is 11.87 MPa. From that model is also possible to obtain derived parameters like the fracture energy rate G_c, which can be calculated from the area below the curve of the friction law $G_c = 0.5 T_u D_c$. The fracture energy rate is of 2.95 MJ m^{-2} for the best dynamic model, which multiplied by the area of the rupture patch gives a total fracture energy of 3.58×10^{14} J, which is within the order found for other intermediate depth earthquakes of similar magnitude (e.g. Díaz-Mojica *et al*. 2014).

4.2 Monte Carlo

The best solution found by the Neighbourhood Algorithm is non-unique. There is a family of different solutions that can explain the observed data with misfits similar to the best solution. The exploration of the solution space by varying all the 10 inverted parameters is computationally expensive, so we only explored the trade-off among the three parameters related to the friction law and stress conditions in the fault: T_e, T_u and D_c, using the Monte-Carlo technique. The other parameters were fixed to those of the best model found by the Neighbourhood Algorithm (Table 1).

The Monte-Carlo inversion of the Jujuy earthquake was performed simulating more than 30 000 models. The distribution of good solutions is an irregular surface inside the 3-D parameter space formed by T_e, T_u and D_c (see Supporting Information Fig. S6a). In order to see the dependence between the terms of κ, we projected our solutions to the plane ($\mu T_u D_c$, $T_e{}^2 L$). Models with misfits lower than 0.48 for the Jujuy earthquake are shown in blue in Fig. 7(a). We observe a linear trend of good solutions, which slightly widens as those parameters increase. This trend indicates that the good models are controlled by the ratio of $T_e{}^2$ to $T_u D_c$, and that the stress drop is not unique for good solutions. In order to compare our results with other earthquakes studied with the same methodology, we also show in Fig. 7 the results obtained by Ruiz & Madariaga (2011) for the 2007 M_w 6.7 Michilla earthquake (red points) occurred in Chile at 43 km depth, and by Ruiz & Madariaga (2013) for the 2008 M_w 6.8 Iwate earthquake (green points) occurred in Japan at 115 km depth, where the points of each one of those earthquakes are also related to misfits lower than 0.48. To adjust and quantify the observed trends, we performed a linear regression with least squares.

From Fig. 7(a), it is possible to conclude that the distributions of good models of the three events share similar values of κ, which can be seen by comparing the slopes obtained for each model distribution. This means that despite the differences in depth of those events, if we consider the entire family of good solutions obtained from the dynamic inversion, the ratio between the terms related to strain energy ($T_e{}^2 L$) and those related to fracture energy ($\mu T_u D_c$) is roughly constant for all the considered events. On the other hand, Fig. 7(b) shows that the proportionality factor between M_o and $T_e L^3$ varies between 1.59 and 2.14 for the three earthquakes. These values are slightly lower than the proportionality factor of the relation

$$M_o = \frac{16}{7} T_e L^3 \tag{3}$$

which was derived for a circular rupture with constant stress drop (Madariaga 1976; Madariaga & Ruiz 2016). The slight difference between the obtained proportionality factors of the events with the value of $c_0 = 16/7$ may be due to the elliptical patch used to model these events and the fact that c_0 was derived using a circular instantaneous rupture model. Despite of this difference, those values are consistent with c_0, showing only a small variability at least in these three earthquakes of similar size.

5 DISCUSSION AND CONCLUSIONS

We studied the rupture process of the 2015 Jujuy earthquake by performing kinematic and dynamic inversions with regional data. The elliptical kinematic and dynamic models were described by 7 and 10 parameters, respectively. The teleseismic inversion shows an agreement with the regional kinematic inversion in terms of rupture velocity. This suggests that the event had subshear rupture propagation around 2.4 and 2.8 km s^{-1}. The geometry of the rupture is well constrained by the teleseismic and regional kinematic and

dynamic inversions, and all suggest a propagation up and southwards from the hypocentre.

We also performed a Monte-Carlo inversion of the frictional parameters involved in the rupture process of the Jujuy earthquake. We found that the good models with misfits $\chi^2 < 0.48$ are strongly controlled by the ratio κ between strain energy and fracture energy, showing a roughly linear distribution between $T_e{}^2L$ and $\mu T_u D_c$. After comparing our results with those of the Michilla and Iwate earthquakes, we found that κ has similar values for each one of them, which would suggest that this parameter is independent of the depth where each event occurred, at least for these earthquakes with similar magnitudes. We also found similar patterns in the ratio between M_o and $T_e L^3$ for all earthquakes, which is not far from the solution derived for an instantaneous circular rupture.

The inverted stress drop of Jujuy earthquake was 11.87 MPa, which is less than the stress drop obtained with the asperity model for Michilla earthquake (Ruiz & Madariaga 2011) and Iwate earthquake inverted with data set 1 (Ruiz & Madariaga 2013), which were 14.97 and 34.25 MPa, respectively. These results show that even if these events have similar rupture size, their dynamic parameters (obtained with the same modelling method) can be different. The fracture energy rate G_c derived from the inversion results, was 2.95 MJ m^{-2} for Jujuy, while for Michilla and Iwate we inferred values of 6.23 and 28.26 MJ m^{-2}, respectively. These results agree with the modelled seismic moment of each event. We observe that for events of similar rupture size, the fracture energy G_c scales with the seismic moment. This means that effective stress and fracture energy scale with each other as expected from the observation that the parameter κ is very similar for all the events considered.

ACKNOWLEDGEMENTS

This research was supported by the Fondo Nacional de Desarrollo Científico y Tecnológico (FONDECYT) No. 11130230 of Comisión Nacional de Investigación Científica y Tecnológica (CONICYT), Chile, and Programa Riesgo Sísmico (Universidad de Chile). CH thanks CONICYT for the scholarship PCHA/MagísterNacional/2014-22140434, and the Departamento de Postgrado y Postítulo de la Vicerrectoría de Asuntos Académicos (Universidad de Chile). We finally thank Luis Franco from OVDAS, Centro Sismológico Nacional (CSN), Integrated Plate boundary Observatory Chile (IPOC), Instituto Nacional de Prevención Sísmica (INPRES) and Incorporated Research Institutions of Seismology (IRIS), who provided the data used in this work.

REFERENCES

Bouchon, M., 1981. A simple method to calculate Green's functions for elastic layered media, *Bull. seism. Soc. Am.,* **71**(4), 959–971.

Cahill, T. & Isacks, B., 1992. Seismicity and shape of the subducted Nazca plate, *J. geophys. Res.,* **97**(B12), 17 503–17 529.

Campus, P. & Das, S., 2000. Comparison of the rupture and radiation characteristics of intermediate and deep earthquakes, *J. geophys. Res.,* **105**(B3), 6177–6189.

Chen, Y., Wen, L. & Ji, C., 2014. A cascading failure during the 24 May 2013 great Okhotsk deep earthquake, *J. geophys. Res.,* **119**(4), 3035–3049.

Comte, D., Pardo, M., Dorbath, L., Dorbath, C., Haessler, H., Rivera, L., Cisternas, A. & Ponce, L., 1994. Determination of seismogenic interplate contact zone and crustal seismicity around Antofagasta, northern Chile using local data, *Geophys. J. Int.,* **116**(3), 553–561.

Coutant, O., 1989. *Programme de simulation numérique AXITRA*, Res. Report LGIT, Grenoble, France.

Di Carli, S., François-Holden, C., Peyrat, S. & Madariaga, R., 2010. Dynamic inversion of the 2000 Tottori earthquake based on elliptical subfault approximations, *J. geophys. Res.,* **115**(B12), doi:10.1029/2009JB006358.

Díaz-Mojica, J., Cruz-Atienza, V.M., Madariaga, R., Singh, S.K., Tago, J. & Iglesias, A., 2014. Dynamic source inversion of the M6.5 intermediate-depth Zumpango earthquake in central Mexico: a parallel genetic algorithm, *J. geophys. Res.,* **119**(10), 7768–7785.

Frohlich, C., 2006. *Deep Earthquakes*, Cambridge Univ. Press.

Houston, H., 2015. *Treatise on Geophysics (Second Edition), Volume 4: Earthquake Seismology*, pp. 329–354, Elsevier.

Houston, H., Benz, H.M. & Vidale, J.E., 1998. Time functions of deep earthquakes from broadband and short-period stacks, *J. geophys. Res.,* **103**(B12), 29 895–29 913.

Husen, S., Kissling, E., Flueh, E. & Asch, G., 1999. Accurate hypocentre determination in the seismogenic zone of the subducting Nazca Plate in northern Chile using a combined on-/offshore network, *Geophys. J. Int.,* **138**(3), 687–701.

Ida, Y., 1972. Cohesive force across the tip of a longitudinal-shear crack and Griffith's specific surface energy, *J. geophys. Res.,* **77**(20), 3796–3805.

Kanamori, H., Anderson, D.L. & Heaton, T.H., 1998. Frictional melting during the rupture of the 1994 Bolivian earthquake, *Science,* **279**(5352), 839–842.

Lomax, A., Virieux, J., Volant, P. & Berge-Thierry, C., 2000. Probabilistic earthquake location in 3D and layered models, in *Advances in Seismic Event Location*, pp. 101–134, eds Thurber, C.H. & Rabinowitz, N., Springer.

Madariaga, R., 1976. Dynamics of an expanding circular fault, *Bull. seism. Soc. Am.,* **66**(3), 639–666.

Madariaga, R. & Olsen, K., 2000. Criticality of rupture dynamics in 3-D, *Pure appl. Geophys.,* **157**(11–12), 1981–2001.

Madariaga, R. & Ruiz, S., 2016. Earthquake dynamics on circular faults: a review 1970–2015, *J. Seismol.,* **20,** 1235–1252.

Peyrat, S. & Favreau, P., 2010. Kinematic and spontaneous rupture models of the 2005 Tarapacá intermediate depth earthquake, *Geophys. J. Int.,* **181**(1), 369–381.

Peyrat, S., Olsen, K. & Madariaga, R., 2001. Dynamic modeling of the 1992 Landers earthquake, *J. geophys. Res.,* **106**(B11), 26 467–26 482.

Poli, P. & Prieto, G., 2014. Global and along-strike variations of source duration and scaling for intermediate-depth and deep-focus earthquakes, *Geophys. Res. Lett.,* **41**(23), 8315–8324.

Poli, P. & Prieto, G.A., 2016. Global rupture parameters for deep and intermediate-depth earthquakes, *J. geophys. Res.,* **121**(12), 8871–8887.

Poli, P., Prieto, G., Rivera, E. & Ruiz, S., 2016. Earthquakes initiation and thermal shear instability in the Hindu-Kush intermediate-depth nest, *Geophys. Res. Lett.,* **43,** 1537–1542.

Ruiz, S. & Madariaga, R., 2011. Determination of the friction law parameters of the M_w 6.7 Michilla earthquake in northern Chile by dynamic inversion, *Geophys. Res. Lett.,* **38**(9), doi:10.1029/2011GL047147.

Ruiz, S. & Madariaga, R., 2013. Kinematic and dynamic inversion of the 2008 Northern Iwate earthquake, *Bull. seism. Soc. Am.,* **103**(2A), 694–708.

Sambridge, M., 1999. Geophysical inversion with a neighbourhood algorithm—I. Searching a parameter space, *Geophys. J. Int.,* **138**(2), 479–494.

Tassara, A. & Echaurren, A., 2012. Anatomy of the Andean subduction zone: three-dimensional density model upgraded and compared against global-scale models, *Geophys. J. Int.,* **189**(1), 161–168.

Tocheport, A., Rivera, L. & Chevrot, S., 2007. A systematic study of source time functions and moment tensors of intermediate and deep earthquakes, *J. geophys. Res.,* **112**(B7), doi:10.1029/2006JB004534.

Twardzik, C., Das, S. & Madariaga, R., 2014. Inversion for the physical parameters that control the source dynamics of the 2004 Parkfield earthquake, *J. geophys. Res.,* **119**(9), 7010–7027.

Vallée, M. & Bouchon, M., 2004. Imaging coseismic rupture in far field by slip patches, *Geophys. J. Int.,* **156**(3), 615–630.

Warren, L.M. & Silver, P.G., 2006. Measurement of differential rupture durations as constraints on the source finiteness of deep-focus earthquakes, *J. geophys. Res.,* **111**(B6), doi:10.1029/2005JB004001.

Wiens, D., 2001. Seismological constraints on the mechanism of deep earthquakes: temperature dependence of deep earthquake source properties, *Phys. Earth planet. Inter.,* **127**(1), 145–163.

Zhan, Z., Kanamori, H., Tsai, V.C., Helmberger, D.V. & Wei, S., 2014. Rupture complexity of the 1994 Bolivia and 2013 Sea of Okhotsk deep earthquakes, *Earth planet. Sci. Lett.,* **385,** 89–96.

SUPPORTING INFORMATION

Supplementary data are available at *GJIRAS* online.

Figure S1. A change in the coordinates that define the hypocentre resulted in different synthetic waveforms in the modelling with regional data. The global misfits between observed and synthetic traces were 0.35, 0.39, 0.59 and 0.83 for the inversion done with our hypocentre, the CSN hypocentre, USGS hypocentre and GEOFON hypocentre, respectively. In this figure are shown the observed traces compared with the synthetic ones obtained from the tests with each hypocentre. These are the traces corresponding to some of the components where the differences are most notorious.

Figure S2. Results of the teleseismic inversion. The hemispheres of the focal mechanism are shown in (a) and (b), where the solutions with low misfits are marked with black dots. The best solutions are shown inside the red square in (b), which are located very close to the plane with dip of 71°. A schematic cross-section of the obtained fault plane and rupture direction is shown in (c). The graph in (d) shows with red dots the stations used as a function of take-off angle and the azimuth with respect to the epicentre.

Figure S3. Comparison between the observed seismograms (in blue) with the synthetic seismograms (in red) of the best model obtained by the kinematic inversion using a filter with frequencies between 0.02 and 0.2 Hz.

Figure S4. Comparison between the observed seismograms (in blue) with the synthetic seismograms (in red) of the best model obtained by the kinematic inversion using a filter with frequencies between 0.02 and 0.25 Hz.

Figure S5. Comparison between the observed seismograms (in blue) with the synthetic seismograms (in red) of the best model obtained by the kinematic inversion using a filter with frequencies between 0.02 and 0.5 Hz.

Figure S6. Results of the dynamic Monte-Carlo inversion of the Jujuy earthquake. Each dot represents a model, and its respective colour is associated with its misfit. The colour scale for misfits was saturated in 1 for both graphics. Models with misfits lower than 0.48 are shown with larger dots. The star in each graphic corresponds to the best solution determined by the Neighbourhood Algorithm. (a) The 3-D space of solutions of the three inverted parameters. (b) Relation of the values of κ and M_o for each one of the tested models in the inversion.

Table S1. Seven inverted parameters that define the kinematic model. The inversion was made using the Neighbourhood Algorithm.